Bubble-Size Distributions and Flow Fields in Bubble Columns

F. Lehr, M. Millies, and D. Mewes
Institute of Process Engineering, University of Hannover, D-30167 Hannover, Germany

Bubble-size distributions and flow fields in bubble columns are calculated numerically. The population balance is simplified and reduced to a balance equation for the average bubble volume. Models developed predict the rate of bubble breakup and coalescence based on physical principles. The flow fields are numerically calculated for bubble columns with cylindrical cross sections using the Euler-Euler method. The newly derived balance equations for the average bubble volumes are implemented into a commercial CFD code. The solutions of the balance equation for high superficial gas velocities result mainly in two fractions: one for the fraction with small and the other for the fraction with large bubble diameters. Both are considered pseudocontinuous phases, in addition to the liquid phase. The calculated flow fields are characterized by several large-scale vortices. The local volume fractions of gas and liquid are locally inhomogeneous and highly time-dependent. The time-averaged flow field is axisymmetric and stationary. The calculated volume fractions, velocities, and bubble-size distributions agree well with existing and previously published experimental results for bubble columns up to 0.3 m in diameter.

Introduction

Bubble columns are used as reactors in a variety of chemical and biochemical processes (Deckwer, 1992; Dudukovic et al., 1999). In bubble columns gases are disperged in liquids in order to obtain large interfacial areas available for heat- and mass-transfer processes. The available commercial methods of computational fluid dynamics (CFD) permit the description of the three-dimensional (3-D) and instationary behavior of the bubbly flow. Through this, various operating conditions and dimensions of the reactor can be considered (Dudukovic et al., 1999; Kuipers and van Swaaij, 1998). The interfacial area density is addressed as one of the key parameters in all simulations. Momentum, mass, and energy transfer occur across the interfaces of the contacting phases. The functionality of two-phase flow in bubble columns depends mainly on these three interfacial transport processes. The interfacial area in bubbly flow has been investigated by Hibiki and Ishii (1999, 2001).

The local interfacial area density is obtained from the local bubble-size distribution. The bubble-size distribution is not stationary in the flow field, but changing locally and with time. Breakup and coalescence of bubbles and mass transfer are governing the local bubble-size distribution. The rates of breakup and coalescence depend on the local flow field. On the other hand, the local bubble-size distribution determines the momentum transfer and affects by this, the local flow field. Flow field and bubble-size distribution are coupled. Nevertheless, the local bubble-size distribution is not included in most of today's simulations of the flow fields in bubble columns.

In spite of the simple construction of bubble columns the flow fields are highly complex. The instantaneous velocity field in bubble columns is shown in Figure 1 based on measurements taken by Fan et al. (1994) applying the particle image velocity (PIV) method. The flow field is characterized by an almost spiral bubble swarm in the center of the column.

Numerical simulations of the flow field in bubble columns are to be realized by using the Euler-Euler or the Euler-Lagrange method. Using the Euler-Lagrange method, the motion of many bubbles is calculated separately. Because of the high numerical effort to calculate the motion of a large

Correspondence concerning this article should be addressed to D. Mewes.

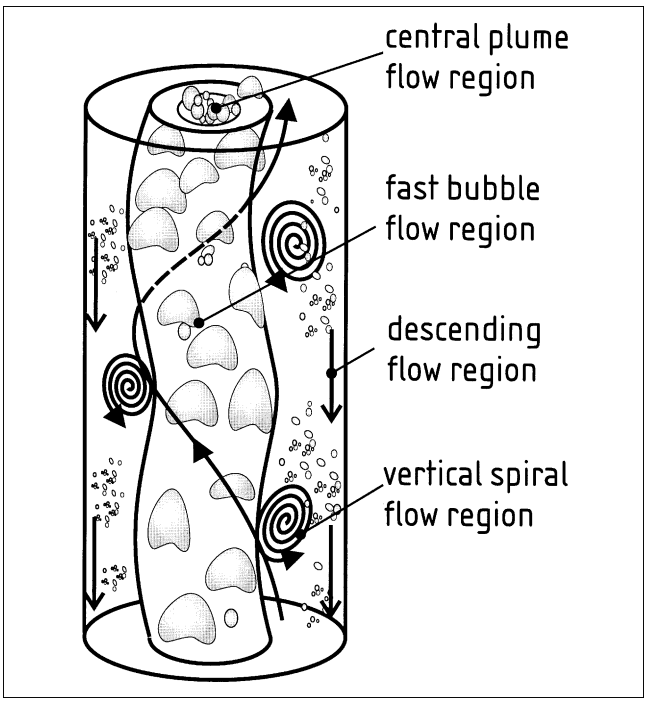

Figure 1. Flow field in a bubble column (Fan et al., 1994).

number of bubbles, the applicability of this method is restricted to low volume fractions of the gaseous phase and low number densities of the bubbles. The numerical effort for the Euler-Euler method is comparatively small. The gaseous phase is considered to be pseudo continuous, and appropriate terms for the interactions between the two phases are taken into account. Both methods lead to the same results if adequate numerical methods are used to solve the resulting equations. A comparison of both methods is given by Sokolichin et al. (1997).

Assuming axisymmetric and stationary flow fields numerical and analytical calculations are carried out for two dimensions by several authors (Torvik and Svendson, 1990; Jacobsen et al., 1997; Saynayal et al., 1999; Thakre and Joshi, 1999; Millies and Mewes, 1992). These models are reasonable for the time averaged flow fields in bubble columns, but they cannot predict the highly instationary and 3-D flow fields which are observed in experiments. Webb et al. (1992) presented the first results from numerical calculations for the time-dependent flow field in bubble columns. They consider the 2-D motion of a rising bubble swarm in a flat bubble column and use the Euler-Lagrange method assuming laminar flow. Results of numerical calculations of the instationary and 3-D flow field in a cylindrical bubble column are presented by Lapin and Lübbert (1995, 1996). They also employ the Euler-Lagrange method. The authors obtain a chaotic like behavior of the two-phase flow. They do not use a turbulence model, but consider the flow field to be laminar.

Sokolichin and Eigenberger (1999) demonstrate that numerical calculations assuming laminar flow do not result in grid independent results. The finer the grid, the more vortices are resolved. This behavior is more typical for turbulent flows. Numerical calculations applying a turbulence model lead to stable and grid independent solutions. The authors perform extensive numerical calculations using a simplified Euler-Euler method. They restrict to 3-D flow fields in bubble columns with a flat rectangular cross section and use local sparging, as well as low volume fractions of the gas. The local turbulence is calculated by a k-ϵ turbulence model. Sokolichin and Eigenberger obtain a good agreement between calculated and measured values by comparing the time-averaged flow field and the time-dependent motion of the rising bubble swarm with their own experimental results.

Similar calculations for the flow fields observed in locally sparged bubble columns with flat rectangular cross sections are performed by several groups: Delnoij et al. (1999) use the Euler-Lagrange method assuming laminar flow. Lain et al. (1999) use a similar method applying a k-ϵ turbulence model. Results from calculations using the Euler-Euler method are presented by Mudde and Simonin (1999) and by Pfleger et al. (1999). Extensive numerical calculations by using the Euler-Euler method are conducted by Pan et al. (1999, 2000). The authors consider the flow in two dimensions only and use fine grids to resolve the shear induced turbulence directly.

Krishna et al. (1999, 2000) perform simulations for the flow field in cylindrical bubble columns using the Euler-Euler method and a k-ϵ turbulence model. For high superficial gas velocities, they consider large bubbles as a third eulerian phase. However, they neglect bubble coalescence and bubble breakup assuming a constant superficial velocity for the large and the small bubbles. The size of the small and large bubbles is considered to be constant. The numerically predicted three-dimensional (3-D) flow field gives satisfying agreement between the measured and the calculated time averaged values of volume fraction and velocity.

The local bubble-size distribution is considered in none of the previous works. In addition most of the simulations are conducted for superficial gas velocities below 0.1 m/s. Only Krishna et al. (2000) present results for superficial gas velocities exceeding 0.1 m/s. Using none of the existing methods, the interfacial area available for heat and mass transfer can be calculated to this point.

Population Balance Equations and Kernel Functions

The local bubble-size distribution may be calculated from the population balance equations. These are transport equations for the number density f of the bubbles, which is defined as the number of bubbles ΔN with volume between v and $v + \Delta v$ per unit volume V and per class width Δv of the size fraction

$$f = \frac{\Delta N}{V \Delta v} \tag{1}$$

The convective transport of bubbles, their coalescence and breakup, as well as mass transfer and an expansion of the gaseous phase are taken into account. A derivation of the population balance, as shown in Table 1, is given by several authors (Valentas and Amundson, 1966; Kocamustafaogullari and Ishi, 1995; Millies and Mewes, 1999) in a similar form.

Table 1. Population Balance Equation

Description	Equation
Temporal change	$\frac{\partial f}{\partial t}$
Convective transport	$+\nabla(f\vec{u}_g) =$
Changes in the gas density	$+\frac{1}{\rho_g}\frac{D\rho_g}{Dt}\frac{\partial}{\partial v}(vf)$
Mass transfer	$-\frac{\partial}{\partial v}\left(\dot{n}A_p\frac{\mu_g}{\rho_g}f\right)$
Breakup of larger bubbles	$+\int_v^\infty r_1(v,v')f(v')dv'$
Breakup of bubbles with vol. v	$-\int_0^v v'r_1(v',v)dv'\frac{f(v)}{v}$
Coalescence of smaller bubbles	$+\frac{1}{2}\int_0^v r_2(v',v-v')f(v')f(v-v')dv'$
Coalescence of bubble with vol. v	$-\int_0^\infty r_2(v',v)f(v')dv'f(v)$

The application of population balance equations for modeling dispersed flows is discussed by Ramkrishna and Mahoney (2001). We restrain our description to a short summary of the terms involving coalescence and breakup.

The breakup of bubbles influences the bubble-size distribution in two ways. On the one hand, new bubbles are produced in one bubble fraction due to the breakup of larger bubbles. On the other hand, the number of bubbles in a bubble fraction decreases because the bubbles do break up themselves. The breakup kernel function

$$r_1(v,v') = \frac{df(v,v')}{f(v)dt} \tag{2}$$

determines the number of bubble fragments with volume v', which are formed per unit time and volume by the breakup of bubbles with volume v. The coalescence of bubbles affects the population balance in two ways. First, new bubbles are formed due to coalescence of smaller bubbles. This way bubbles with volume v' have to coalesce with bubbles of volume v-v'. Secondly, the number of bubbles of volume v' decreases because some of the bubbles coalesce with other bubbles of any size. We consider only binary coalescence (Millies and Mewes, 1999). The coalescence of more than two bubbles at the same time is considered as a series of binary coalescences. $r_2(v',v)$ is called a coalescence kernel function and is used to predict the probability of two bubbles with volumes v' and v to coalesce resulting in a change in the number density of bubbles by

$$r_2(v',v) = \frac{df(v+v')d(v+v')}{f(v')f(v)dv'dvdt}. \tag{3}$$

To solve the population balance equations, the coalescence and breakup kernel functions must be known. The population balance equations provide the mathematical framework in order to describe how coalescence and breakup affect the bubble-size distribution. The probability that bubbles coalesce or break is specified by the two kernel functions. In order to formulate them, the interaction of bubbles with other bubbles and with the turbulent flow field have to be considered. These phenomena are described in detail by Fan (1989) and by Fan and Tsuchiya (1990).

Breakup of Bubbles

The breakup of bubbles is investigated in turbulent flow fields by several groups (Walter and Blanch, 1986; Hesketh et al., 1991; Wilkinson et al., 1993) applying high-speed cameras. The authors agree about the mechanisms leading to breakage. The bubbles are usually deformed by the turbulent flow field and stretched in one direction. This leads to a necking that contracts further, resulting finally in the breakage. For calculation of the bubble-size distribution, the frequency of the bubble breakups has to be specified. In addition the size of the bubbles that are formed during the breakage process, the so-called daughter size distribution, has to be known. For calculation of the breakup kernel function, we make the following assumptions:

(1) The breakup of a bubble in a turbulent flow field is due to the arrival of eddies of different length scales onto the surface of the bubbles (Walter and Blanch, 1986; Lee et al., 1987; Luo and Svendsen, 1996).

(2) Only the binary breakup into two daughter bubbles is considered (Walter and Blanch, 1986; Hesketh et al., 1991; Wilkinson et al., 1993).

(3) The breakup of a bubble is determined by the balance between the interfacial force of the bubble surface and the inertial force of the colliding eddy. The interfacial forces depend on the shape of the bubble and on the size of the resulting bubble fragments. Immediately before the breakage, the bubbles are locally nearly cylindrical. The force balance gives

$$\frac{1}{2}\rho_f u_\lambda^2 = 2\frac{\sigma}{d'} \tag{4}$$

u_λ denotes the turbulent eddy velocity and d' denotes the diameter of the smaller resulting bubble fragment, ρ_f is the liquid density, and σ is the surface tension.

(4) Only eddies with length scales smaller than the bubble diameters can induce breakage. Larger eddies lead to bubble transport instead (Lee et al., 1987; Luo and Svendsen, 1996; Prince and Blanch, 1990). For the same reason, the length scale of the eddy has to be larger than the diameter of the smaller resulting bubble fragment. This gives the simple relationship

$$d' \le \lambda \le d \tag{5}$$

where λ is the length scale of the eddy and d is the bubble diameter before breakage.

Following Luo and Svendsen (1996), the breakup kernel function is calculated from the frequency of arriving eddies onto the surface of the bubble and from the probability that collisions lead to breakage

$$r_1(v',v) = \int_{d'}^{d}\omega(v,\lambda)P(\lambda,v',v)d\lambda. \tag{6}$$

$\omega(v,\lambda)$ denotes the number of collisions between a bubble with the volume $v = \pi d^3/6$ and an eddy with length scale λ.

$P(\lambda,v',v)$ denotes the probability that this collision leads to breakage and to the formation of a daughter bubble with size $v' = \pi d'^3/6$.

The collision frequency $\omega(v,\lambda)$ of eddies of length scale λ with a bubble of diameter d is expressed analogous to the kinetic gas theory by

$$\omega(v,\lambda) = \frac{\pi}{4}(\lambda + d)^2 \bar{u}_\lambda n_\lambda. \tag{7}$$

Assuming that isotropic turbulence is at least on the length scale of the bubbles, the turbulent velocity $\bar{u}_\lambda$ of an eddy of size λ can be calculated in the inertial subrange by a formula given by Hinze (1975)

$$\bar{u}_\lambda = \sqrt{2}\,(\epsilon\lambda)^{1/3} \tag{8}$$

ϵ is the turbulent dissipation rate. The number of eddies per unit volume n_λ of size between λ and $\lambda + d\lambda$ is obtained from the energy spectrum in the inertial subrange of turbulence by

$$n_\lambda = \frac{C}{\lambda^4}, \quad \text{with } C = \frac{9}{2}\frac{2^{1/3}}{(\pi)^{5/3}} = 0.8413. \tag{9}$$

Equation 9 is valid only in the inertial subrange of turbulence. This limitation has no influence on breakup rates, since smaller eddies have not caught enough energy to overcome the interfacial forces. Mudde et al. (1997) use the LDA method to measure the energy spectrum of the turbulence in bubble columns. For high wave numbers, they obtain a decrease of the turbulent energy proportional to $k^{-5/3}$ in accordance with the theory of isotropic turbulence. These findings support the applicability of Eq. 9.

The probability that collisions between eddies and bubbles result in breakages is obtained from the force balance (Eq. 4). The size of the resulting bubble fragments depends on the kinetic energy of the eddy. Equation 8 gives only the mean turbulent velocity of eddies with length scale λ. In reality the velocities follow a normal distribution around this mean value (Hinze, 1975). Therefore, the breakage probability is

$$P(\lambda,v',v) = \frac{4}{\pi}\frac{\sigma}{\rho_f}\frac{1}{\epsilon^{2/3}\lambda^{2/3}}\frac{1}{d'^4}\exp\left(-\frac{2\sigma}{\rho_f}\frac{1}{\epsilon^{2/3}\lambda^{2/3}}\frac{1}{d'}\right). \tag{10}$$

The force balance (Eq. 4) is formulated with the diameter d' of the smaller resulting bubble fragment. Thus, Eq. 10 is only valid for the smaller bubble fragment with volumes in the range $0 \le v' \le v/2$. For the larger bubble fragment $v/2 < v' \le v$, we obtain $P(\lambda,v',v) = P(\lambda,v - v',v)$.

Utilizing Eqs. 6 to 10 yields in the kernel function for breakage

$$r_1(v',v) = \int_{d'}^{d} \sqrt{2}\,C\frac{\sigma}{\rho_f\epsilon^{2/3}d'^4}\frac{(\lambda+d)^2}{\lambda^{13/3}}\exp\left(-\frac{2\sigma}{\rho_f\epsilon^{2/3}d'}\frac{1}{\lambda^{2/3}}\right)d\lambda \quad \text{for } 0 \le v' \le v/2$$

$$r_1(v',v) = r_1(v - v',v) \quad \text{for } v/2 < v' \le v \tag{11}$$

The integral in Eq. 11 can be expressed as a sum of incomplete Γ-functions resulting in analytical expressions for the breakup kernel function r_1, the breakup frequency f_z, and the daughter size distribution β

$$r_1(v',v) = \beta(v,v')f_z(v). \tag{12}$$

In comparison Eqs. 10 and 11 are difficult to be evaluated, but they can be replaced in good approximation by Eq. 12. Therefore, Eqs. 10, 11, and 12 are made dimensionless using the length and time scales

$$L = \left(\frac{\sigma}{\rho_f}\right)^{3/5}\frac{1}{\epsilon^{2/5}} \quad \text{and} \quad T = \left(\frac{\sigma}{\rho_f}\right)^{2/5}\frac{1}{\epsilon^{3/5}} \tag{13}$$

resulting in the dimensionless bubble diameter, eddy length scale, bubble volumes, dimensionless breakup kernel function, breakup frequency and dimensionless daughter size distribution

$d^* = \frac{d}{L}$	dimensionless bubble diameter
$\lambda^* = \frac{\lambda}{L}$	dimensionless eddy diameter
$v^* = \frac{v}{L^3}$	dimensionless bubble volume
$v'^* = \frac{v'}{L^3}$	dimensionless daughter-bubble volume
$r_1^*(v'^*,v^*) = r_1(v',v)L^3T$	dimensionless kernelfunction for breakup
$f_z^* = f_zT$	dimensionless breakage frequency
$\beta^*(v'^*,v^*) = \beta(v',v)L^3$	dimensionless daughter-bubble size distribution after breakage

(14)

The dimensionless breakup frequency is written as

$$f_z^* = 0.5 d^{*5/3} \exp\left(- \frac{\sqrt{2}}{d^{*3}} \right). \quad (15)$$

The dimensionless daughter size distribution is described by a lognormal distribution which gives

$$\beta^*(v'^*, v^*) = \frac{6}{\pi^{3/2} d'^{*3}} \frac{\exp\left\{ - \frac{9}{4} \left[\ln(2^{2/5} d'^*) \right]^2 \right\}}{\left\{ 1 + \mathrm{erf}\left[\frac{3}{2} \ln(2^{1/15} d^*) \right] \right\}}$$

$$\text{for } 0 \le v'^* \le \frac{v^*}{2} \quad (16)$$

and

$$\beta^*(v'^*, v^*) = \beta^*(v^* - v'^*, v^*) \text{ for } \frac{v^*}{2} < v'^* \le v^*. \quad (17)$$

In Eqs. 15 and 17 there are no empirical parameters which have to be adjusted to experimental results. The breakup frequency increases with increasing bubble diameter, increasing dissipation rate, increasing density of the liquid phase, and decreasing surface tension. Equal sized breakage is preferred for small bubbles, because the interfacial forces are high, and, according to Eq. 4, the breakage into two equal sized bubbles is easiest. As the size of the parent bubbles increases, unequal breakage is preferred. The number of eddies decreases rapidly with increasing length scale of the eddies (see Eq. 9). Therefore, large bubbles primarily collide with smaller eddies leading to breakage into one smaller and one larger bubble.

Coalescence of Bubbles

Coalescence of bubbles occurs in turbulent flow in three steps (Chesters, 1991). First, bubbles collide and trap a small amount of liquid between them. This liquid film has to drain until film rupture occurs resulting in coalescence. Otherwise, the bubbles bounce back without coalescing. The probability for a collision to result in coalescence is referred to as coalescence efficiency. It is influenced strongly by the composition of the liquid phase and is reduced for liquids with additives or mixtures of liquids in comparison to pure liquids. This effect is called coalescence inhibition.

The objective of our own experimental investigations is to determine under which conditions collisions of two bubbles result in coalescence or bouncing. The experimental facility is given in Figure 2. The liquid is flowing vertically downwards inside of a channel 0.225 m in length with a rectangular cross section. The cross-sectional area widens from 0.028 m × 0.028 m at the entrance to 0.060 m × 0.060 m at the bottom outlet as the liquid flow is getting downward. This results in a decrease of the average liquid velocity. The velocity profiles are equalized throughout the entrance cross section by the application of an insert with hexagonal channels inside. Near the bottom cross section, bubbles are injected by a capillary. They are of different sizes according to the injected gas volume. The bubbles move countercurrently inside the downwards flowing liquid and rise up to a cross section where there is an equilibrium of the interacting forces. The liquid flow is circulated by a pump and adjusted to the velocities of the rising bubbles by a valve. In countercurrent flow of downward flowing liquid and upward rising bubbles the swarm is fixed locally in the experiments. A high-speed video camera is used to observe the motion of the bubbles with the help of mirrors from two simultaneous perpendicular views. The pictures are analyzed automatically using digital image processing techniques. For each collision of bubbles, it is detected whether the collision results in coalescence or bouncing. The form and size of the bubbles which are simplified and described as ellipsoids, as well as their velocities, are calculated from the images given in Figure 3.

The experimental results for distilled water and air are shown in Figure 4. Whether a collision results in coalescence

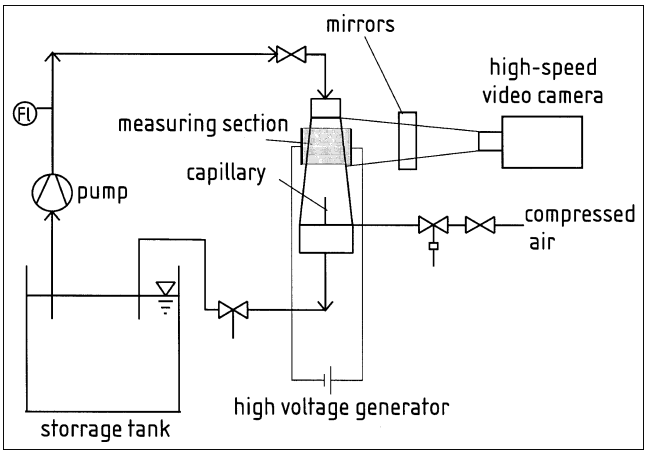

Figure 2. Apparatus for the investigation of bubble coalescence.

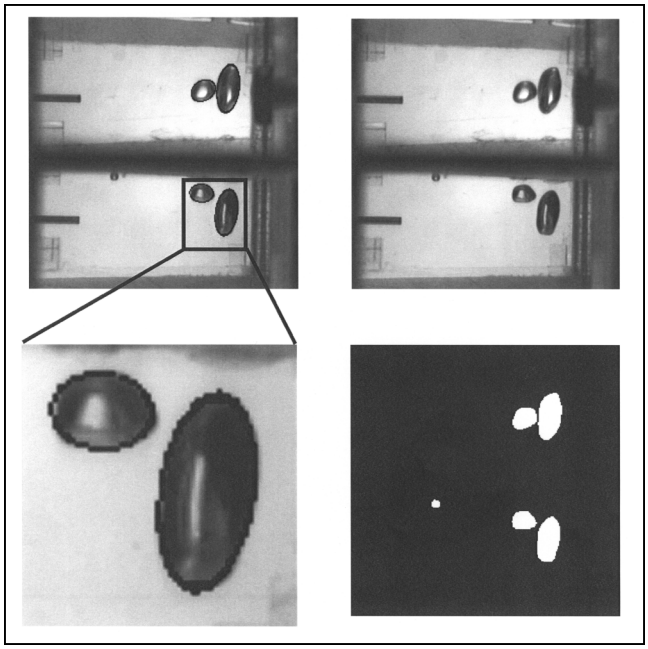

Figure 3. Image processing for the investigation of bubble coalescence.

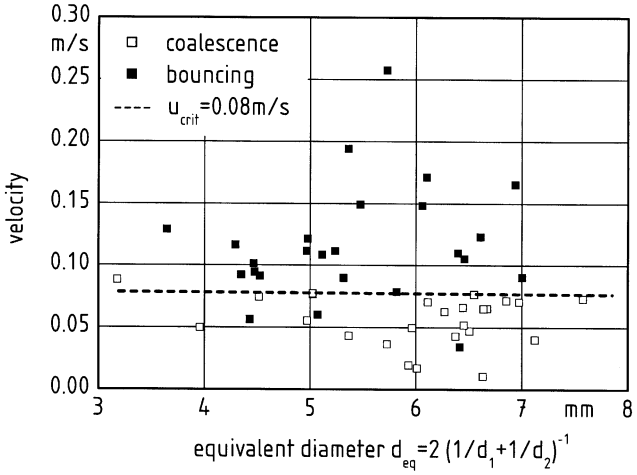

Figure 4. Coalescence efficiency as a function of the bubble diameter and of the relative velocity of approach for distilled water-air.

or bouncing depends on the relative velocity of an approach perpendicular to the surface of contact and on the equivalent bubble diameter. According to Chesters (1991), the equivalent bubble diameter is defined as

$$d_{\mathrm{eq}} = 2\left(\frac{1}{d_1} + \frac{1}{d_2}\right)^{-1} \tag{18}$$

d_1 and d_2 denote the diameters of the two colliding bubbles. The outcome of a collision depends only on the relative velocity of the approach perpendicular to the surface of contact. The maximum velocity resulting in coalescence is called critical velocity. For the distilled water and air, we obtain from the experiments described above the critical velocity $u_{\mathrm{crit}} = 0.08$ m/s. It does not depend on the size of the bubbles.

The coalescence kernel function is stated here to be calculated from the product of the collision frequency and the coalescence efficiency. The former is calculated as the product of the collision cross sectional area $\pi/4(d_1 + d_2)^2$ and the characteristic velocity u'.

Collisions are considered that arise from turbulent fluctuations and from the difference in rise velocities of bubbles of different size. For the first case, the characteristic velocity is assumed to be the turbulent eddy velocity with the length scale of the bubbles. Smaller eddies do not contain sufficient energy to significantly affect the bubble motion, while much larger sized eddies will transport groups of bubbles. For the second case, the characteristic velocity corresponds to the difference in rise velocities of the bubbles. The characteristic velocity is expressed as

$$u' = \max\left(\sqrt{2}\,\epsilon^{1/3}\sqrt{d_1^{2/3} + d_2^{2/3}}, |\vec{u}_1 - \vec{u}_2|\right) \tag{19}$$

Collisions only result in coalescence which occur with a relative velocity of approach perpendicular to the surface of contact lower than the critical velocity. This velocity depends on the angle of approach under which the two bubbles collide. Since the relative motion of the bubbles towards each other is determined by the turbulence in the liquid phase. The assumption is made that the relative probability for a collision has to be equal for all steradians. Thus, we obtain for the coalescence kernel function

$$r_2(v', v) = \frac{\pi}{4}(d_1 + d_2)^2 \min(u', u_{\mathrm{crit}}) \exp\left[-\left(\frac{\alpha_{\max}^{1/3}}{\alpha^{1/3}} - 1\right)^2\right]. \tag{20}$$

The last term in Eq. 20 reflects the limited range of the turbulent fluctuations affecting the motion of the bubbles. This range is considered a normal distribution with $\lambda = d$ as the mean value. α denotes the volume fraction of the bubbles, and $\alpha_{\max} = 0.6$ denotes the maximum packing density of the bubbles (Millies and Mewes, 1999).

The turbulent fluctuation velocity usually exceeds in bubble columns the critical velocity for coalescence of typical bubble sizes. In Eq. 20 only this critical velocity for coalescence has to be considered. The coalescence efficiency itself depends only on the chemical composition of the liquid and the gaseous phase. Investigations of Millies and Mewes (1999) support that the coalescence efficiency is for pure liquids a constant value and is independent of the physical parameters of the liquid. Thus, the critical velocity for coalescence is in pure liquids $u_{\mathrm{crit}} = 0.08$ m/s. We obtained this value from our experiments with distilled water. The coalescence inhibition for liquids with additives or mixtures of liquids causes lower critical velocities. A possible method to obtain critical velocities for liquids mixtures from simple experiments is suggested by the next paragraph.

Simplified Balance Equation

The derived kernel functions for bubble breakup and coalescence are used to solve the population balance equation numerically. For this purpose, a simplified flow field is considered. It is characterized by zero superficial liquid velocity, a constant volume fraction of the gas, and a constant turbulent dissipation rate. As a result, the time-dependent evolution of bubble-size distributions is obtained numerically from the population balance equation given in Table 1. For high superficial gas velocities, bimodal bubble-size distributions with a large and a small bubble fraction are calculated. The accumulated volume fraction of the gas is depicted in Figure 5 for different times. After short times, an almost stable size distribution of small bubbles is reached, whereas the larger bubbles keep on growing. The size distribution becomes bimodal. Large and small bubbles can be distinguished clearly. For longer times, the volume fractions of small and large bubbles remain almost constant.

The kernel functions for breakup and coalescence are valid up to high volume fractions of the gas. The formation and growth of large bubbles under these conditions are reproduced in the calculations. This is not possible so far with any of the previous known methods.

The population balance equations may be simplified according to Millies and Mewes (1999). This simplification is explained as follows. The population balance is solved numerically for different volume fractions, dissipation rates and

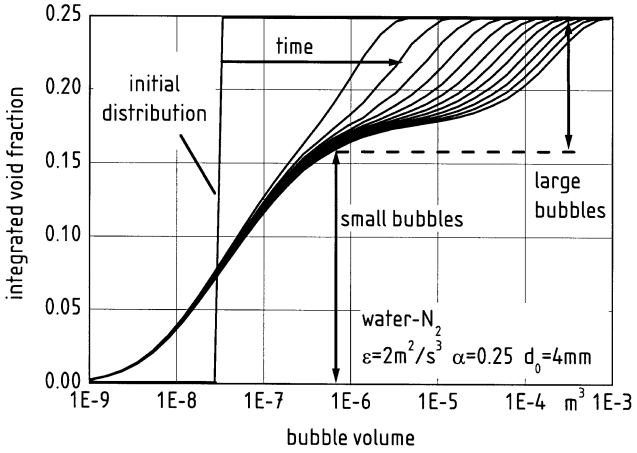

Figure 5. Bimodal bubble-size distribution for high superficial gas velocities.

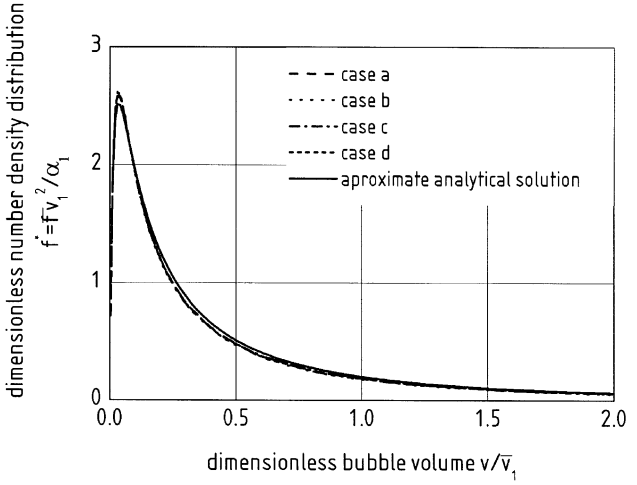

Figure 6. Number density distributions of the small bubbles.

(a) $\rho_f = 998$ kg/m^3 $\sigma = 0{,}0727$ kg/s^2 $\alpha = 0{,}25$ $\epsilon = 2$ m^2/s^3; (b) $\rho_f = 998$ kg/m^3 $\sigma = 0{,}0727$ kg/s^2 $\alpha = 0{,}4$ $\epsilon = 4$ m^2/s^3; (c) $\rho_f = 998$ kg/m^3 $\sigma = 0{,}02$ kg/s^2 $\alpha = 0{,}25$ $\epsilon = 2$ m^2/s^3; (d) $\rho_f = 500$ kg/m^3 $\sigma = 0{,}02$ kg/s^2 $\alpha = 0{,}25$ $\epsilon = 2$ m^2/s^3.

material properties. The calculated number density distributions are depicted in Figure 6 by applying the dimensionless form with the help of the average bubble volume $\bar{v}_1$, respectively, $\bar{v}_2$ and the volume fraction α_1, respectively, α_2 of the small and large bubble fraction

$$\hat{f} = \hat{f}_1 + \hat{f}_2 = \frac{\bar{v}_1^2}{\alpha_1} f_1 + \frac{\bar{v}_2^2}{\alpha_2} f_2. \tag{21}$$

The dimensionless number density distributions deviate from each other very little, while the average bubble volume changes by more than one decade. The dimensionless number density distribution of the small bubble fraction is approximated by a lognormal distribution

$$\hat{f}_1 = \sqrt{\frac{2}{\pi}}\,\frac{1}{3\hat{v}_1}\exp\left[-\frac{2}{9}\ln\left(e^{9/8}\hat{v}_1\right)\right] \qquad \text{with } \hat{v}_1 = \frac{v}{\bar{v}_1}. \tag{22}$$

The dimensionless number density distribution of the large bubble fraction is approximated by an exponential distribution

$$\hat{f}_2 = \exp(-\hat{v}_2) \qquad \text{with } \hat{v}_2 = \frac{v}{\bar{v}_2}. \tag{23}$$

The number density distributions Eqs. 22 and 23 are used to evaluate the population balance equation. Integration of the population balance equation (Table 1) over all bubble volumes results in balance equations for the average bubble volume and the volume fractions of large and small bubbles. For the derivation, it is recognized that the average bubble volume of the small bubbles is small in comparison to the average bubble volume of the large bubbles $\bar{v}_1 \ll \bar{v}_2$. The resulting balance equations are given in Table 2.

Knowing the average bubble volumes and the volume fractions, the number density distribution of the bubbles is obtained from Eqs. 22 and 23. For low volume fractions, large bubbles are not relevant. The system of equations is reduced to one single balance equation for the average bubble volume.

For high superficial gas velocities and bimodal bubble-size distributions, the relative volume fraction of large and small bubbles remains almost constant. A dynamic equilibrium between coalescence and breakup is reached. The same amount of gas goes from the large bubble to small bubble fraction due to the breakup of large bubbles, and from the small bubble to the large bubble fraction due to coalescence of small and large bubbles. The volume fraction of the small bubbles under these conditions is approximated by

$$\alpha_{1\mathrm{GGW}} = 0.065\left(\frac{\sigma}{\rho_f}\epsilon\right)^{1/5}\frac{1}{u_{\mathrm{crit}}} \tag{24}$$

The volume fraction of small bubbles does not depend on the integral volume fraction. The volume fraction of the small bubbles decreases with decreasing coalescence efficiency. Fewer large bubbles are formed. The volume fraction of the small bubbles increases slightly with increasing turbulence intensity. The breakup of large bubbles is intensified.

For complex liquids which show coalescence inhibition, the critical velocity for coalescence is obtained by rearranging Eq. 24

$$u_{\mathrm{crit}} = 0.065\left(\frac{\sigma}{\rho_f}\epsilon\right)^{1/5}\frac{1}{\alpha_{1\mathrm{GGW}}} \tag{25}$$

The critical velocity for coalescence is calculated from the volume fraction of small bubbles for developed flow for high superficial gas velocities. The volume fraction of small bubbles can be obtained from experiments. Equation 25 gives a possibility to quantify the coalescence efficiency of complex liquids with the help of experiments.

Table 2. Simplified Balance Equations

Variable	Balance Equation
Avg. vol. of small bubbles	$\frac{\partial \bar{v}_1}{\partial t} + \vec{u}_{g1}\nabla(\bar{v}_1) = Z_1\bar{v}_1 - 0.3463 r_2(\bar{v}_1,\bar{v}_1)\alpha_1 - \frac{1}{\rho_g}\frac{D\rho_g}{Dt}\bar{v}_1 + \dot{n}a_{p1}\frac{\mu_g}{\rho_g}\frac{\bar{v}_1}{\alpha_1}$
Avg. vol. of large bubbles	$\frac{\partial \bar{v}_2}{\partial t} + \vec{u}_{g2}\nabla(\bar{v}_2) = Z_2\bar{v}_2 - 0.4250 r_2(\bar{v}_2,\bar{v}_2)\alpha_2 + 0.9024 r_2(\bar{v}_2,5\bar{v}_1)\alpha_1 - \frac{1}{\rho_g}\frac{D\rho_g}{Dt}\bar{v}_2 + \dot{n}a_{p2}\frac{\mu_g}{\rho_g}\frac{\bar{v}_2}{\alpha_2}$
Vol. fraction of small bubbles	$\frac{\partial \alpha_1 \rho_g}{\partial t} + \nabla(\alpha_1 \rho_g \vec{u}_{g1}) = Z_2\,\rho_g\,\alpha_2 - 0.9024 r_2(\bar{v}_2,5\bar{v}_1)\rho_g\frac{\alpha_2\alpha_1}{\bar{v}_2} - 3.1043 r_2(\bar{v}_1,\bar{v}_1)\rho_g\frac{\alpha_1^2}{\bar{v}_2} + \dot{n}a_{p1}\,\mu_g$
Vol. fraction of large bubbles	$\frac{\partial \alpha_2 \rho_g}{\partial t} + \nabla(\alpha_2 \rho_g \vec{u}_{g2}) = -Z_2\,\rho_g\,\alpha_2 + 0.9024 r_2(\bar{v}_2,5\bar{v}_1)\rho_g\frac{\alpha_2\alpha_1}{\bar{v}_2} + 3.1043 r_2(\bar{v}_1,\bar{v}_1)\rho_g\frac{\alpha_1^2}{\bar{v}_2} + \dot{n}a_{p2}\,\mu_g$
	$Z_1 = 0.6082\left(\frac{\rho_f}{\sigma}\right)^{7/5}\epsilon^{19/15}\bar{v}_1^{5/9}\exp\left[-\frac{0.8565}{\sqrt{\bar{v}_1}}\left(\frac{\sigma}{\rho_f}\right)^{9/10}\frac{1}{\epsilon^{3/5}}\right]$
	$Z_2 = 0.2545\left(\frac{\sigma}{\rho_f}\right)^{2/5}\epsilon^{1/15}\frac{1}{\bar{v}_2^{4/9}}$
	$r_2(v_i,v_j) = \frac{\pi}{4}\left[\left(\frac{6}{\pi}v_i\right)^{1/3} + \left(\frac{6}{\pi}v_j\right)^{1/3}\right]^2 \min(u',u_{krit})\exp\left[-\left(\frac{\alpha_{max}^{1/3}}{\alpha^{1/3}} - 1\right)^2\right]$

Comparison with Experimental Data

The calculation method for bubble-size distributions is applied to several experimentally investigated systems. By this, the breakup kernel functions are validated against experimental data for the breakup of single bubbles in turbulent flow fields. Since it is difficult to measure the coalescence kernel functions directly, calculated bubble-size distributions are compared with experimental data instead.

Lasheras et al. (1999) study the breakup of air bubbles in a turbulent water jet. The LDA technique is used to measure the turbulent energy spectrum in the jet to calculate the local dissipation rate. Bubbles are injected into the core of the jet, and the spatial evolution of the bubble-size distribution is measured. The bubbles are subdivided into different sized classes. The number of bubbles in the class with the largest bubbles decreases only due to the breakup of these bubbles. From this decrease, the breakup frequency is calculated in dependence of the dissipation rate.

Lasheras et al. obtain a decrease of the breakup frequency with increasing bubble diameter. This unexpected behavior results from an incorrect evaluation of the experimental values. The authors choose too large size classes. Not every breakup of a bubble means that the bubble leaves the size class. If the size distribution of the resulting bubble fragments is known, the mistake can be corrected. This is obtained from Eqs. 16 and 17. The corrected dimensionless size distribution is shown in Figure 7 as a function of the dimensionless bubble diameter. In addition experimental results from Wilkinson et al. (1993) for the breakup of bubbles in turbulent pipe flow are shown. In the experimental investigations the bubble diameter and the dissipation rate are varied. The dependence of the breakup frequency on these parameters is described by Eq. 15 in accordance with the experiments.

The bubble-size distribution in bubble columns can be calculated independent of CFD simulations if an equilibrium between coalescence and breakup is reached. The dissipation rate is calculated by the ratio of the specific energy introduced by the gas and the mass of the liquid in the bubble column

$$\epsilon = \frac{j_g g \rho_f (1-\alpha_g)}{\rho_f (1-\alpha_g)} = j_g g \tag{26}$$

j_g denotes the superficial gas velocity, and g the gravitational acceleration. The calculated bubble-size distributions are given in Figure 8 together with the measured distribution by Grienberger and Hofmann (1992) and Schrag (1976). Measured and calculated values are in agreement. Thus, we conclude that the coalescence frequency can be calculated using Eq. 20.

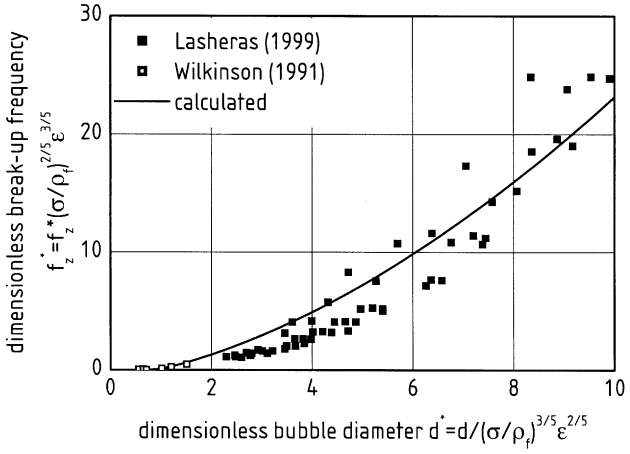

Figure 7. Breakup frequency of experimental results: Lasheras et al. (1999) vs. Wilkinson (1991).

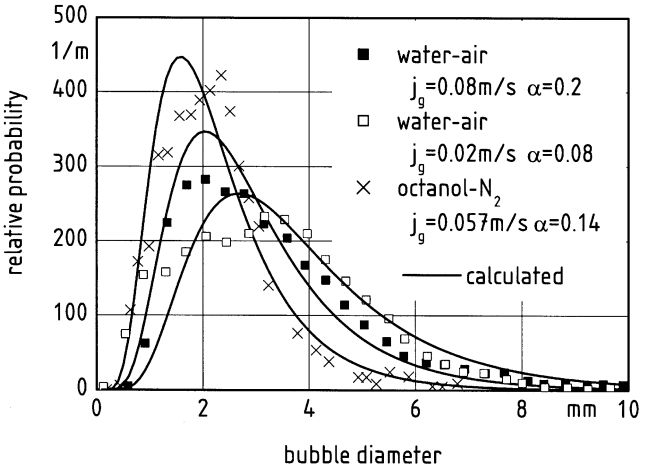

Figure 8. Bubble-size distribution for the equilibrium between coalescence and breakup of experimental results: Grienberger and Hofmann (1992) vs. Schrag (1976).

Grund uses the dynamic gas disengagement method to measure the volume fractions of small and large bubbles in bubble columns. The measured volume fractions of the small bubbles are depicted in Figure 9 together with calculated values from Eq. 24. The dissipation rate is calculated from Eq. 26. For the small volume fraction, the volume fraction of the small bubbles is calculated from $\alpha_1 = j_g/\bar{u}_{g1}$. The volume fraction of the small bubbles increases slightly with increasing superficial gas velocity. Besides water and methanol, Grund (1988) uses also a mixture from paraffins (Ligroin) as a liquid phase which shows coalescence inhibition. If coalescence inhibition is not taken into account, the calculated volume fraction of small bubbles is much too low. With coalescence inhibition, the calculated and measured values are in good agreement. From the measured bubble volume fractions, the critical velocity for coalescence is calculated using Eq. 25 to be 0.043 m/s.

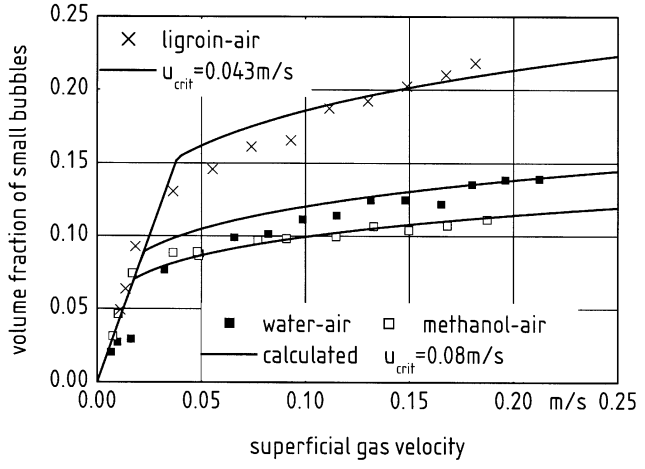

Figure 9. Volume fraction of small bubbles in a bubble column, comparison with experimental results by Grund (1988).

Grund (1988) also uses a photographic technique to measure the interfacial area density of the bubbles. Only if coalescence inhibition is considered measured and calculated values compare well. Thus, Eq. 25 can be used to quantify the effect of coalescence inhibition. The described method for interfacial area density calculation is also valid for systems where coalescence inhibition is important.

Numerical Calculations

The results of the numerical calculations are the time-dependent and 3-D velocity and volume fraction fields of the continuous phase, as well as those of the dispersed phase in cylindrical bubble columns. The local bubble-size distributions are considered by the transport equation for bubbles of small and large sizes which are given in Table 1. The numerical calculations are performed with a commercially available CFD-code. The Euler-Euler-model is applied to all three phases. It takes into account that, besides the liquid phase, both bubble sizes have to be considered as independent phase flows when the superficial gas velocities are high. The Reynolds stress tensor is calculated from a k-ϵ-model. The velocity fields are considered to be laminar for the gaseous phases. The mass and momentum balance equations are derived by Drew (1983). The mass balance equation for the liquid phase is

$$\frac{\partial \alpha_f \rho_f}{\partial t} + \nabla\left(\alpha_f \rho_f \vec{u}_f\right) = -\dot{n}a_{p1}\,\mu_g - \dot{n}a_{p2}\,\mu_g. \qquad (27)$$

For the small and large size bubble fractions, the appropriate equations are given in Table 2. The three momentum balance equations are

$$\frac{\partial \alpha_k \rho_k \vec{u}_k}{\partial t} + \nabla\left[\alpha_k \rho_k \vec{u}_k \vec{u}_k - \mu_k\left(\nabla\vec{u}_k + \nabla\vec{u}_k^T\right) + \frac{2}{3}\mu_k \nabla\cdot\vec{u}_k\,\delta\right] = -\alpha_k \nabla p + \vec{M}_{kf} + \alpha_k \rho_k g \qquad (28)$$

with k as indice for all three phases. The closure equations for the interfacial momentum transfer between the two dispersed phase flows and the liquid flow is calculated from Clift et al. (1978)

$$\vec{M}_{kf} = \frac{3}{4}\rho_f \frac{\alpha_k}{ds_k} C_D \,|\,\vec{u}_k - \vec{u}_f\,|\left(\vec{u}_k - \vec{u}_f\right) \qquad (29)$$

with

$$C_D = \max\left\{\frac{24}{Re}(1+0.1Re^{0.75})\min\left[\max\left(0.44, \frac{2}{3}Eo^{1/2}\right), \frac{8}{3}\right]\right\}$$

$$Re = \frac{\rho_f\,|\,\vec{u}_f\,|\,ds_k}{\mu_f}$$

$$Eo = \frac{g(\rho_f - \rho_g)ds_k}{\sigma}. \qquad (30)$$

The lift and the virtual mass force terms are omitted because of the large interactions taking place between the turbulent

flowing liquid and the rising bubbles. The local bubble-size distribution is obtained from the solution of the additional balance equations for the average bubble volumes of the small and large bubble fraction, as given in Table 2. The sauter mean diameter of both bubble fractions

$$ds_1 = 1.613\bar{v}_1^{1/3} \text{ and } ds_2 = 1.374\bar{v}_2^{1/3} \tag{31}$$

is used to calculate the interphase transfer terms between both phases and the bubble induced turbulence. The turbulent Reynolds stress in the liquid phase is calculated using a k-ϵ turbulence model. The balance equations for the turbulent kinetic energy k_f and the rate of dissipation ϵ_f are

$$\frac{\partial \alpha_f \rho_f k_f}{\partial t} + \nabla\left[\alpha_f \rho_f \vec{u}_f k_f - (\mu_f + \mu_t)\nabla k_f\right] = \alpha_f (P_f - \rho_f \epsilon_f)$$

$$\frac{\partial \alpha_f \rho_f \epsilon_f}{\partial t} + \nabla\left[\alpha_f \rho_f \vec{u}_f \epsilon_f - (\mu_f + \mu_t)\nabla \epsilon_f\right] = \alpha_f \frac{\epsilon_f}{k_f}(1.44 P_f - 1.92 \rho_f \epsilon_f)$$

$$\text{with } P_f = (\mu_f + \mu_t)\nabla \vec{u}_f \cdot \left(\nabla \vec{u}_f + \nabla \vec{u}_f^T\right) - \frac{2}{3}\nabla \cdot \vec{u}_f\left[(\mu_f + \mu_t)\nabla \cdot \vec{u}_f + \rho_f k_f\right]. \tag{32}$$

The application of the k-ϵ-model was recently successfully done by Sokolichin and Eigenberger (1999) for two phase flows with low volume fractions of gas. The turbulent viscosity is

$$\mu_t = 0.09 \rho_f \frac{k_f^2}{\epsilon_f}. \tag{33}$$

For high gas volume fractions, the bubble induced turbulence has to be considered besides the shear induced turbulence. The bubble induced turbulence is considered using the model of de Bertodano et al. (1994). The turbulent kinetic energy k_f and the rate of dissipation ϵ_f are calculated from shear and bubble induced terms

$$k_t = k_f + k_g = k_f + \frac{1}{4}\alpha_1 |\vec{u}_{g1}|^2 + \frac{1}{4}\alpha_2 |\vec{u}_{g2}|^2$$

$$\epsilon_t = \epsilon_f + \epsilon_g = \epsilon_f + \frac{\vec{M}_{1f}}{\rho_f}|\vec{u}_{g1}| + \frac{\vec{M}_{2f}}{\rho_f}|\vec{u}_{g2}| \tag{34}$$

whereas the bubble induced viscosity change according to the model of Sato et al. (1981) is neglected compared to the much larger shear induced viscosity calculated from Eq. 33.

The additional Eqs. 27–34 are implemented into the commercial code CFX-4.2 and solved using the finite volume method. A block structured grid is used with volume elements with edges of 1–2 cm in length. For the discretization of the convective terms, a second-order TVD-schema (Sokolichin and Eigenberger, 1999) is used. The time integration is done with an implicit Euler-method. Time steps between 0.01 s and 0.05 s are used.

The instationary flow fields in cylindrical bubble columns without internals are calculated. The gas is dispersed at the bottom of the column by a sieve plate to equal sized bubbles. The free surface at the top of the column is replaced by modeling a semi-permeable wall. In this way the gas can leave the system, whereas the liquid surface acts as a frictionless wall for the liquid. The liquid is considered to leave the system through an overflow at the periphery of the column.

Low Superficial Gas Velocities

Results are presented for the flow field in a bubble column with 0.29 m diameter and 4.425 m height and 0.02 m/s superficial gas velocity. The initial bubble diameter is 3 mm. Large bubbles are not present under these conditions. The instantaneous volume fraction of the gas and the instantaneous flow field of liquid and gas are shown in Figure 10. The flow field of the liquid is visualized using a texture. The color scales with the vertical liquid velocity. In addition the trajectories of a number of bubbles in the 3-D flow field are shown. The chosen time is 100 s after startup.

In the flow field of the continuous phase a rising and meandering bubble swarm with high volume fractions can be observed. The flow field of the liquid phase is characterized by several large-scale vortices. The length scale of these vortices corresponds to the column diameter. The local liquid velocities reach up to ± 0.5 m/s. The areas with a high upward velocity correspond with the areas of high local volume fractions, whereas the local volume fraction are low in areas with a high downward velocity. One part of the bubbles is carried downwards with the vortices and recirculates. Other bubbles are trapped in the upward flowing part in the middle of the column and rise with a high velocity. These high velocity differences result in a broad residence time spectrum of the gas phase.

The flow field is not stationary, but locally changing with time. The local volume fractions of the gas and the flow field of the liquid phase are shown in Figure 11 and Figure 12 for different times with a temporal distance of 1 s. The bubble swarm makes almost a spiral rotating movement. The large-scale vortices move through the column and determine the form and the motion of the bubble swarm. The flow field is shown as a vertical slice through the centerline of the column. Vortices can disappear and reenter the plane because of their 3-D motion.

The instationary character of the flow field is analyzed further in Figure 13. Here, the instantaneous liquid velocity is shown for one local point in the upper part of the column. The velocity is shown for the time interval from 150 s to 250 s after startup. The time-averaged liquid velocities of 0.01 m/s result from much higher fluctuating velocities. From a fast fourier transform applied to this time series, the dominating frequencies of about 0.1 to 0.15 Hz are obtained. These frequencies correspond to time periods of less than 10 s indicating one rotation of the bubble swarm, as shown in Figure 11. The motion is not periodic, but has chaotic character.

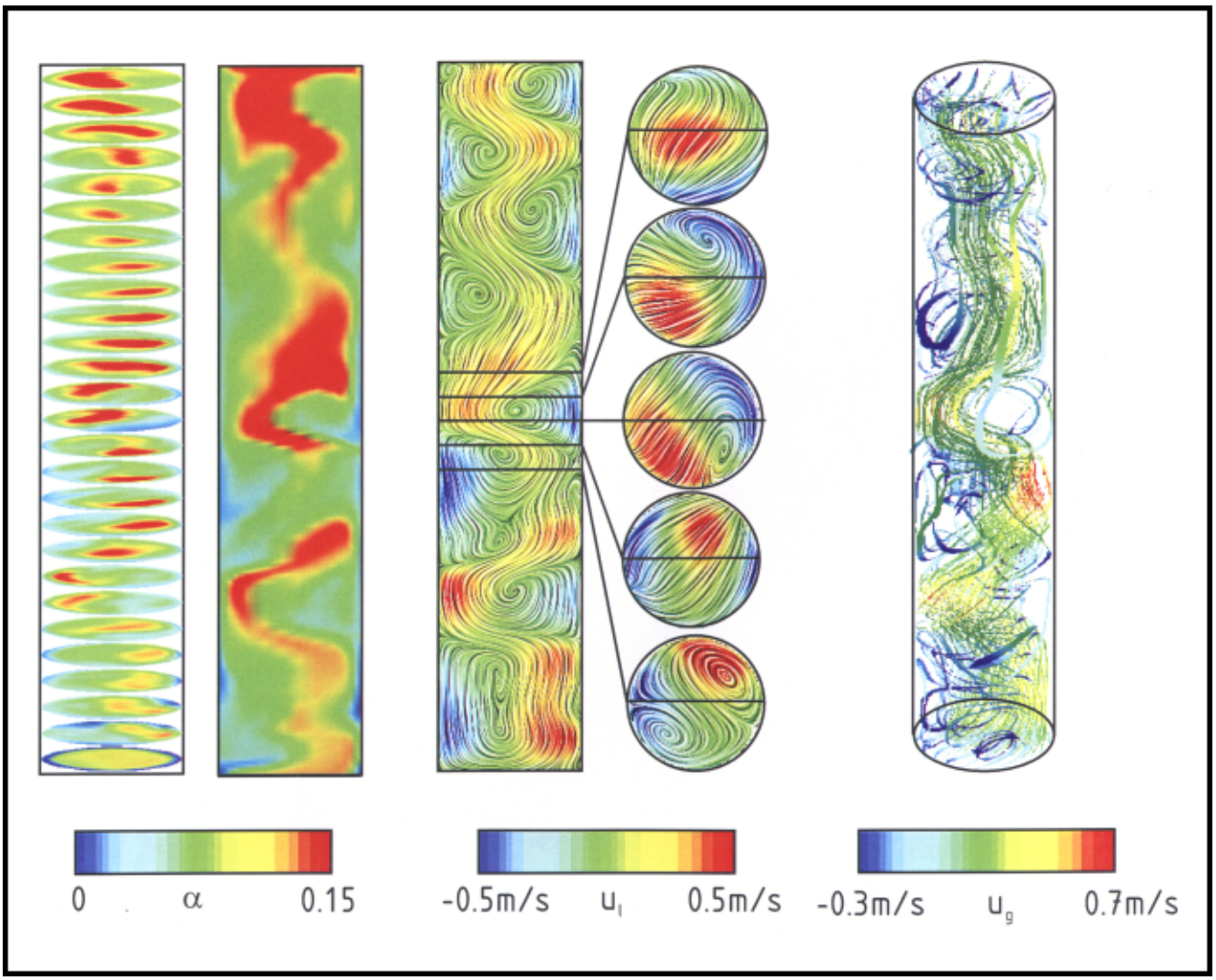

Figure 10. Instantaneous volume fraction and instantaneous flow fields of liquid and gas, $D = 0.29$ m, $H = 4.425$ m, $j_g = 0.02$ m/s.

High Superficial Gas Velocities

The results presented so far are typical for the flow fields in bubble columns for low superficial gas velocities. For higher superficial gas velocities, large fast rising bubbles appear. In the simulations small and large bubbles are considered as separated phases within their own flow fields. The calculations are done for all three phases: liquid, small, and large bubbles. The initial bubble diameter at the bottom sieve plate is 2 mm for the small bubbles and 2 cm for the large bubbles. The results for the flow fields are calculated for 0.1 m/s as superficial gas velocity and bubble column dimensions of 0.15 m diameter and 1.5 m height. The instantaneous local volume fractions and the instantaneous volume averaged diameters of the small and large bubbles are shown in Figure 14. In Figure 15 the flow fields of the liquid and the large and small bubbles are shown. The integral column averaged volume fraction of small bubbles is 0.098 and that of large bubbles is 0.089. The local volume fractions reach up to 0.2 for the small bubbles and up to 0.25 for the large bubbles. The flow field of the liquid phase is characterized by several vortices. The vortices do not extend over the whole column diameter. The liquid flows spirally upwards in the middle of the column. The small bubbles are partially trapped in the vortices and flow downward near the wall. The large bubbles are not captured by the vortices due to their high rise velocities. Therefore, the large bubbles rise primarily near the center of the column, whereas the small bubbles are much more equally distributed. The average bubble diameter of the small bubbles decreases from about 4 mm at the bottom of the column to about 2 mm at the top. The average diameter of the large bubbles increases from about 2 cm near the bottom to about 5 cm at the top of the column.

Comparison with Experimental Results

The time-averaged phase velocity fields are axisymmetric and stationary. The liquid flows upward in the center of the column and downward near the wall. The volume fraction is

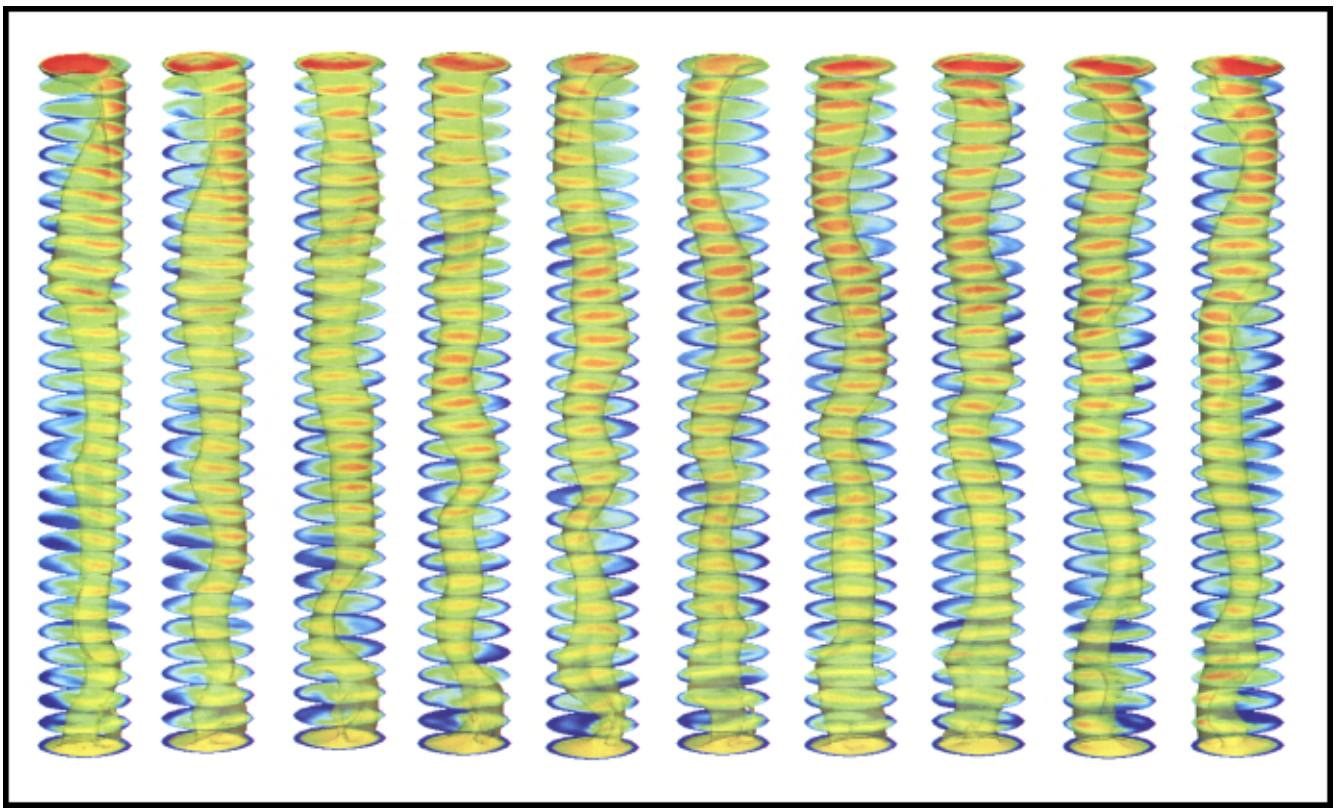

Figure 11. Time-dependent volume fraction of the gas, $D = 0.29$ m, $H = 4.425$ m, $j_g = 0.02$ m/s.

The time difference between two consecutive pictures is $\Delta t = 1$ s.

highest in the middle of the column and lowest at the wall. In Figure 16 to Figure 18 the time averaged axial velocity fields for the low superficial gas velocity of 0.02 m/s are compared with experimental results by Grienberger and Hofmann (1992) and for the high superficial velocity of 0.1 m/s with experimental results by Hills (1974).

The radial profiles of the time-averaged volume fraction are shown in Figure 16. The volume fraction of the large bubbles has a parabolic profile with a maximum in the middle of the column. The volume fraction of the small bubbles is almost constant over the radius except for the near wall region. The radial profiles of the time-averaged liquid veloci-

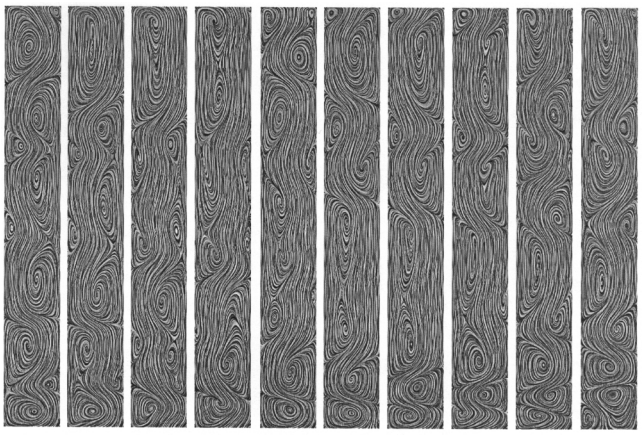

Figure 12. Time-dependent flow field of the liquid, $D = 0.29$ m, $H = 4.425$ m, $j_g = 0.02$ m/s.

The time difference between two consecutive pictures is $\Delta t = 1$ s.

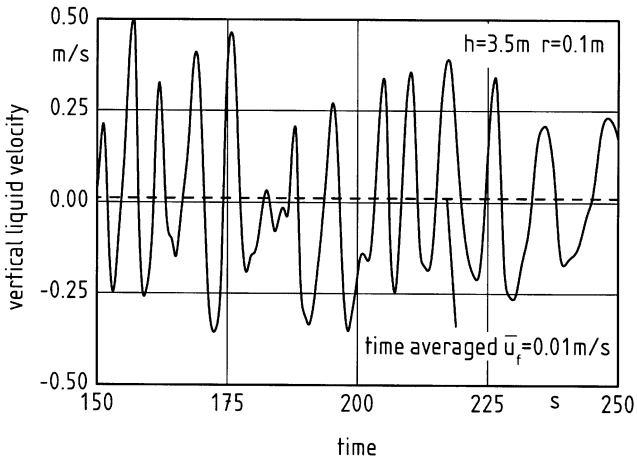

Figure 13. Time series of the liquid velocity, $D = 0.29$ m, $H = 4.425$ m, $j_g = 0.02$ m/s.

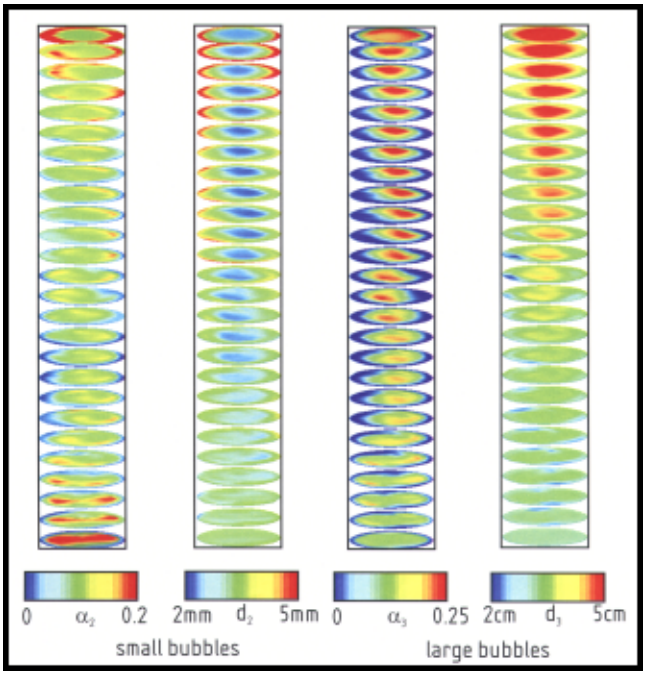

Figure 14. Instantaneous volume fractions and average bubble diameters of small and large bubbles, $D = 0.15$ m, $H = 1.5$ m, $j_g = 0.10$ m/s.

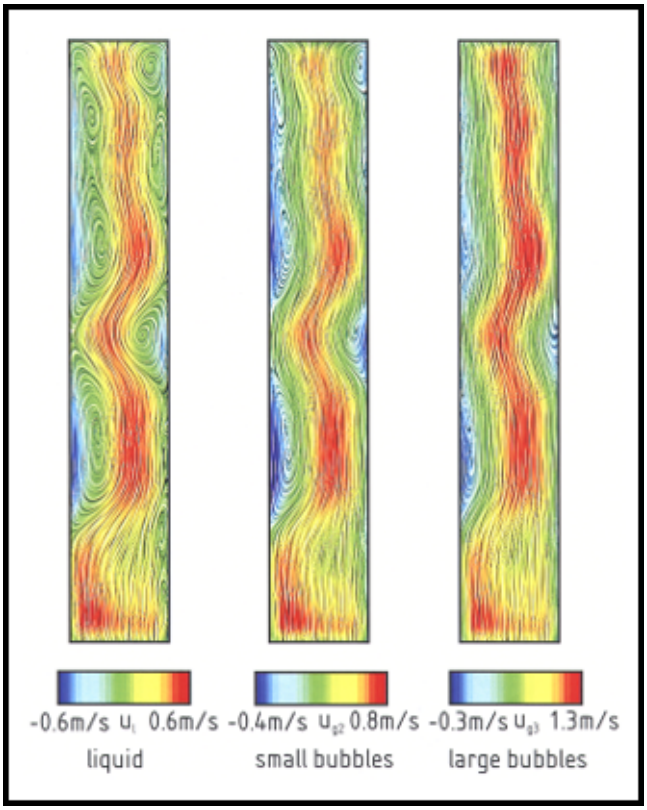

Figure 15. Instantaneous flow fields of the liquid and the small and large bubbles, $D = 0.15$ m, $H = 1.5$ m, $j_g = 0.10$ m/s.

ties are shown in Figure 17. The time-averaged vertical velocities are much smaller than the instantaneous ones.

The radial profiles of the time averaged turbulent fluctuating velocity and the time-averaged dissipation rate are shown in Figure 18. The turbulent fluctuating velocity is calculated from the turbulent kinetic energy

$$u'_f = \sqrt{\frac{2}{3}k_f} \tag{35}$$

and compared with experimental results by Grienberger and Hofmann (1992). Experimental results for the dissipation rate are not available. Integration of the local dissipation rates over the whole flow field yield an averaged dissipation rate of 0.19 m^2/s^3, whereas according to Eq. 34 a dissipation rate of

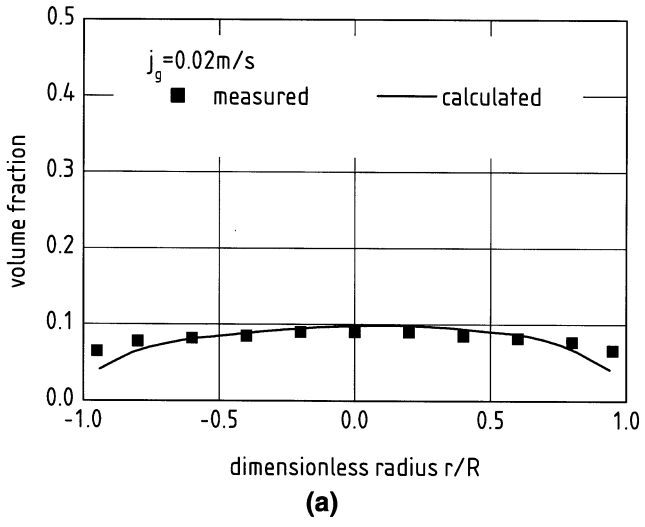

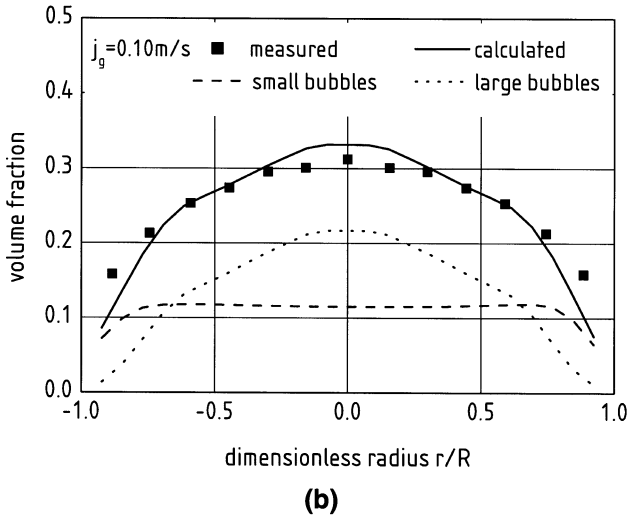

Figure 16. Time-averaged volume fractions of experimental results: (a) Grienberger (1992); (b) Hills (1974).

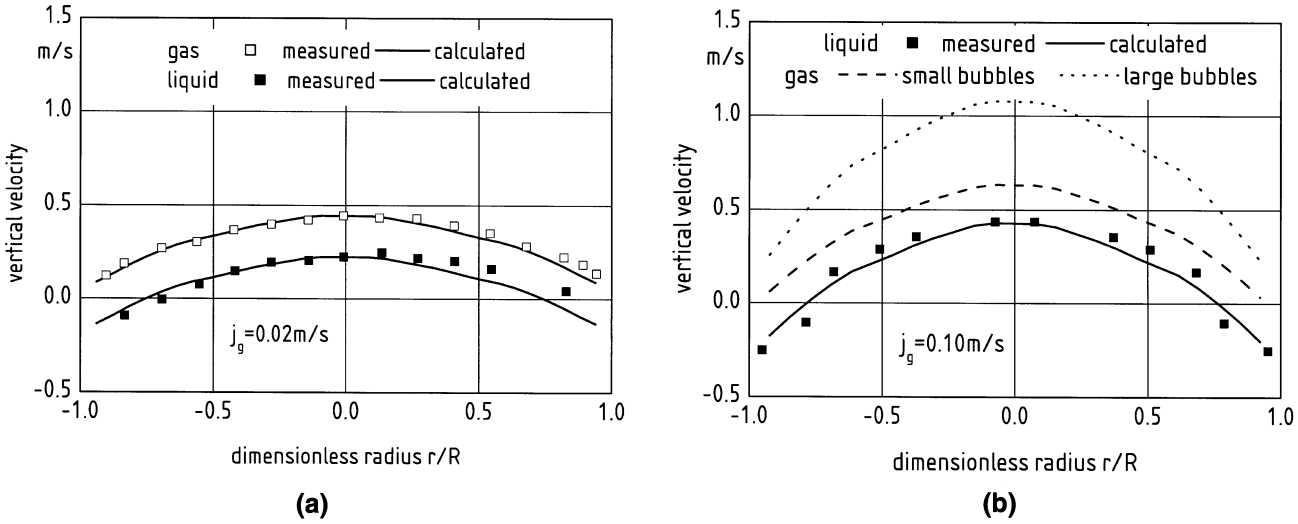

Figure 17. Time-averaged vertical velocities of experimental results: (a) Grienberger (1992); (b) Hills (1974).

0.196 m^2/s^3 is calculated from the power introduced by the gas. The numerical calculations give the order of magnitude of the turbulent fluctuating velocity, as well as the order of magnitude of the dissipation rate.

The integral volume fractions and the integral interfacial area densities are shown in Figure 19 in dependency of the superficial gas velocity for a bubble column with 0.15 m diameter and 1.5 m height. The calculated volume fractions for 0.02 m/s to 0.17 m/s superficial gas velocity are compared with experimental results by Grund (1988). The integral volume fraction of the gas phase, as well as that of the large bubbles increase with increasing superficial gas velocity. The integral interfacial area density increases also with increasing superficial gas velocity. The interfacial area density of the large bubbles is small compared to the interfacial area density of the small bubbles.

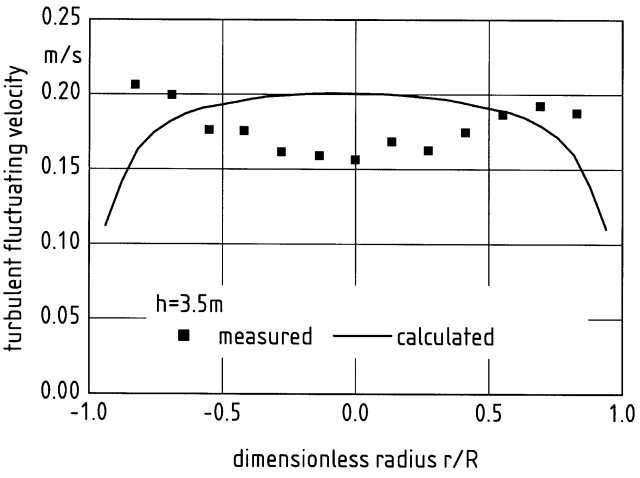

Figure 18. Time-averaged turbulent fluctuating velocities, comparison with experimental results by Grienberger (1992).

Sensitivity to the Bubble-Size Distributions

Two examples are presented to illustrate the influence of the bubble-size distributions onto the flow fields in bubble columns. First, for a superficial gas velocity of 0.02 m/s, the diameters of the bubbles leaving the sparger were selected to be initially 1 mm and 5 mm. The results are compared to those from calculations for bubbles with the constant diameter of 1 mm in the whole column. The last case corresponds to a system with strong coalescence inhibition. For the second example with a superficial gas velocity of 0.06 m/s, results from simulations with and without large bubbles are compared. All calculations are done for a bubble column of 0.15 m diameter and 1.5 m height.

For the first example, the instantaneous average bubble diameters and the instantaneous interfacial area densities are shown in Figure 20. Starting with an initial bubble diameter of 5 mm, the average bubble diameter is almost constant in the whole flow field. The minimum bubble diameter is 4 mm, whereas the maximum bubble diameter reaches up to 6 mm. The averaged bubble diameter in the whole column is 5.4 mm. Starting with an initial bubble diameter of 1 mm, the average bubble diameter increases with increasing height in the column up to 5.3 mm. The bubble diameter varies strongly in the lower part of the column. The averaged bubble diameter in the whole column is 3.8 mm.

The different bubble-size distributions result in very different interfacial area densities available for heat and mass transfer. Starting with an initial bubble diameter of 5 mm, the integral interfacial area density amounts to 49.7 m^{-1}. Starting with an initial diameter of 1 mm, a much higher integral interfacial area density of 87.1 m^{-1} is reached. The main differences are located near the sparger with local interfacial area densities up to 510 m^{-1}. Simulations with a constant bubble diameter of 1 mm lead to an integral interfacial area density of 406 m^{-1} and local interfacial area densities of up to 810 m^{-1}.

The radial profiles of the time-averaged volume fraction are shown in Figure 21. The calculated values are compared

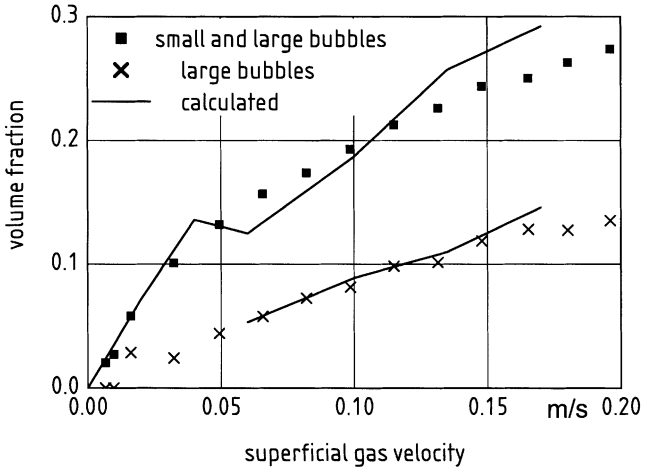

Figure 19a. Integral volume fractions, comparison with experimental results by Grund (1988).

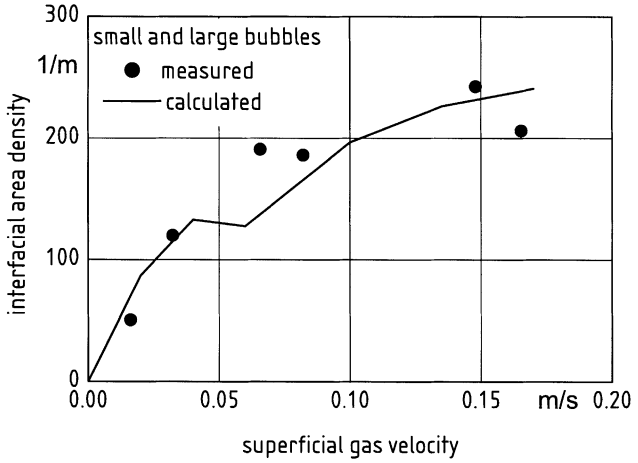

Figure 19b. Integral interfacial area density, comparison with experimental results by Grund (1988).

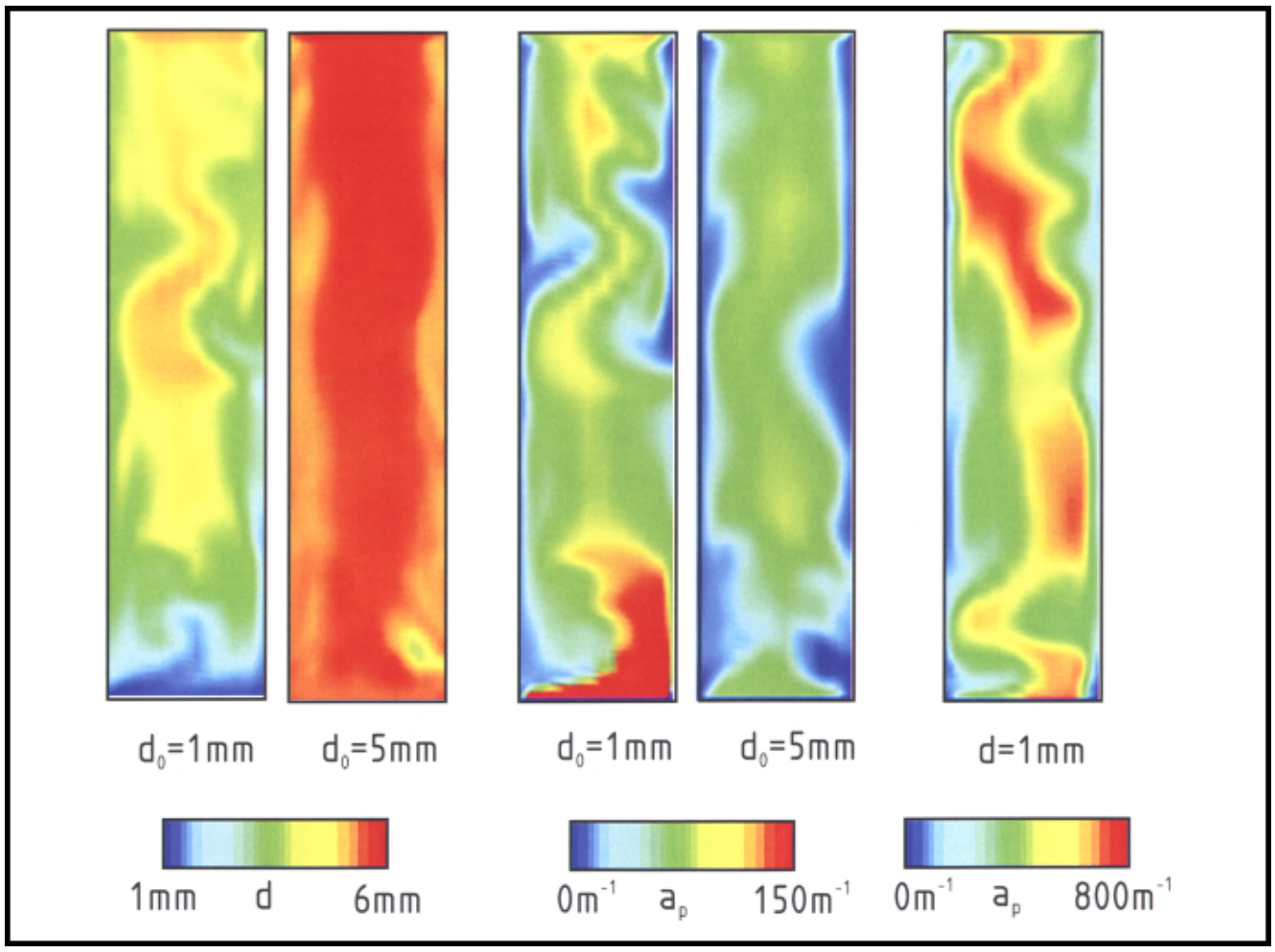

Figure 20. Instantaneous average bubble diameter and instantaneous interfacial area density, importance of the bubble-size distribution, $D = 0.15$ m, $H = 1.5$ m, $j_g = 0.02$ m/s.

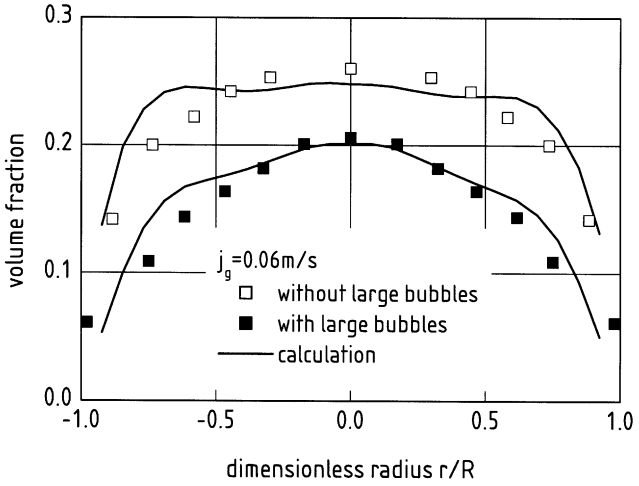

Figure 21a. Time-averaged volume fractions, $D = 0.15$ m, $H = 1.5$ m, $j_g = 0.06$ m/s, comparison with experimental results by Hills (1974).

with experimental results by Hills (1974). Smaller bubbles lead to higher volume fractions. The integral volume fraction is 0.0583 for the initial bubble diameter of 5 mm and 0.072 for an initial bubble diameter of 1 mm. For the constant bubble diameter of 1 mm, the integral volume fraction reaches 0.093. The calculated radial profiles of the time-averaged volume fractions for the initial bubble diameter of 5 mm are in agreement with the experimental results. Unfortunately, Hills does not monitor the bubble diameters in his experiments.

Conclusions

Bubble-size distributions and flow fields in bubble columns are calculated numerically. A population balance equation is used to predict bubble-size distributions by modeling the breakup and coalescence processes of bubbles. In addition the variation in volume of each individual bubble, due to mass transfer or due to expansion of the gaseous phase, is included in the calculations. Based on physical principles, a new model for the breakup of bubbles in a turbulent flow field is developed that leads to the breakup kernel function. The rate of bubble breakup, as well as the size distribution of the resulting bubble fragments, is obtained as a result. The critical bouncing velocity for coalescence of bubbles is investigated experimentally. Its value determines the coalescence kernel function and to the rate of coalescence between bubbles.

As a solution to the population balance equation, bimodal bubble-size distributions with small and large bubbles are obtained for large superficial gas velocities. The self-similarity of the calculated bubble-size distributions is utilized in order to reduce the population balance to balance equations for the average bubble volumes, as well as the volume fractions of the small and large bubbles. These equations can be implemented into existing CFD codes for the calculations of interfacial area densities which are necessary in order to calculate the momentum, mass, and energy fluxes.

The phase velocity fields are calculated numerically for cylindrical bubble columns without internals using the Euler-Euler method. The newly derived balance equations for the averaged small and large bubble volume fractions are implemented into a commercial CFD code.

Both bubble fractions are considered as pseudo continuous phases in addition to the liquid phase. The two-phase flow fields are characterized by several large-scale vortices. The volume fractions of gas and liquid are very inhomogeneous and highly time-dependent. The time-averaged axial velocity fields of both phases are radial symmetrical and stationary. The calculated volume fractions, velocities, and bubble sizes are compared with existing experimental results for bubble columns up to 0.3 m in diameter.

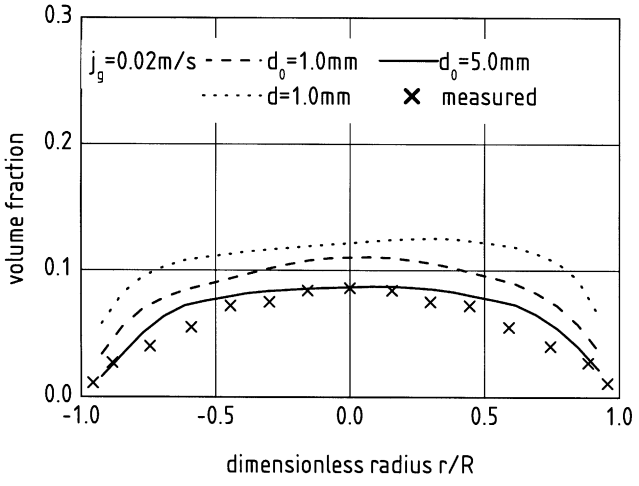

Figure 21b. Time-averaged volume fractions, $D = 0.15$ m, $H = 1.5$ m, influence of bubble-size distribution, $j_g = 0.02$ m/s, comparison with experimental results by Hills (1974).

Acknowledgments

The authors wish to thank the German Research Foundation (DFG) for the financial support within the Priority Program "Analysis, Modelling and Numerical Prediction of Two-Phase Flow."

Notation

a_p = surface area density, m^{-1}
A_p = surface area of a bubble, m^2
C_D = drag coefficient
d = bubble diameter, m
d_{eq} = equivalent bubble diameter, m
ds = sauter mean diameter, m
D = bubble column diameter, m
f = number density distribution, m^{-6}
f_z = breakup frequency, s^{-1}
g = gravitational constant, ms^{-2}
h = bubble column height, m
j = superficial velocity, m/s
k = turbulent kinetic energy, m^2/s^2
L = characteristic length scale, m
$\vec{M}_{kf}$ = interphasial force per unit volume, $kg \cdot m^{-2} \cdot s^{-2}$
n = number density, m^{-3}
n_λ = number density of eddies with length scale λ, m^{-4}
$\dot{n}$ = molar flux, $kmol/m^2/s$
N = number
P = breakup probability, m^{-3}
r = radius, m
r_1 = breakup kernel function, $m^{-3}s^{-1}$
r_2 = coalescence kernel function, m^3/s

R = bubble column radius, m
t = time, s
T = characteristic time scale, s
$\vec{u}$ = velocity vector, m/s
u_{crit} = critical velocity for coalescence, m/s
u' = turbulent fluctuating velocity, m/s
v = bubble volume, m^3
$\bar{v}$ = average bubble volume, m^3
V = volume, m^3

Greek letters

α = volume fraction
β = daughter size distribution, m^{-3}
δ = Kronnecker-delta
Δ = difference
ϵ = dissipation rate, m^2/s^3
λ = length scale of an eddy, m
μ_g = molar mass, kg/kmol
ρ = density, kg/m^3
σ = surface tension, kg/s^2
τ = shear stress, $kg/m/s^2$
ω = collision frequency of a bubble and an eddy of length scale λ, $m^{-1}s^{-1}$

Indices

0 = initial value
1 = small bubbles
2 = large bubbles
f = liquid
g = gas
λ = vortex
t = turbulent
GGW = equilibrium
$'$ = daughter bubble
* = dimensionless variable
$\hat{}$ = scaled variable

Literature Cited

Chesters, A. K., "The Modelling of Coalescence Processes in Fluid-Liquid Dispersions: A Review of Current Understanding," *Inst. Chem. Engnrs.*, **69**, 259 (1991).

Clift, R., J. R. Grace, and M. E. Weber, *Bubbles, Drops and Particles*, Academic Press, New York (1978).

de Bertodano, M. L., R. T. Lahey, and O. C. Jones, "Development of a k-ϵ-Model for Bubbly Two-Phase Flow," *J. Fluids Eng.*, **116**, 128 (1994).

Deckwer, W.-D., *Bubble Column Reactors*, Wiley, Chichester, U.K. (1992).

Degaleesan, S., M. Dudukovic, and Y. Pan, "Experimental Study of Gas-Induced Liquid-Flow Structures in Bubble Columns," *AIChE J.*, **47**, 1913 (2001).

Delnoij, E., J. A. M. Kuipers, and W. P. M. van Swaaij, "A Three Dimensional CFD Model for Gas-Liquid Bubble Columns," *Chem. Eng. Sci.*, **54**, 2217 (1999).

Drew, D. A., "Mathematical Modelling of Two-Phase Flow," *Ann. Rev. Fluid. Mech.*, **15**, 261 (1983).

Dudukovic, M. P., F. Larachi, and P. L. Mills, "Multiphase Reactors —Revisited," *Chem. Eng. Sci.*, **54**, 1975 (1999).

Fan, L.-S., *Gas-Liquid-Solid Fluidization Engineering*, Butterworth, Stoneham, MA (1989).

Fan, L.-S., and K. Tsuchiya, *Bubble Wake Dynamics in Liquids and Liquid-Solid Suspensions*, Butterworth, Stoneham, MA (1990).

Fan, L.-S., R. C. Chen, and J. Reese, "Flow Structure in a Three-Dimensional Bubble Column and Three-Phase Fluidised Bed," *AIChE J.*, **40**, 1093 (1994).

Grienberger, J., and H. Hofmann, "Investigation and Modelling of Bubble Columns," *Chem. Eng. Sci.*, **47**, 2215 (1992).

Grund, G., "Hydrodynamische Parameter und Stoffaustauscheigenschaften in Blasensäulen mit organischen Medien," PhD Thesis, Universität Oldenburg, Germany (1988).

Hesketh, R. P., A. W. Etchells, and T. W. F. Russell, "Bubble Breakage in Pipeline Flow," *Chem. Eng. Sci.*, **46**, 1 (1991).

Hibiki, T., and M. Ishii, "Experimental Study on Interfacial Area Transport in Bubbly Two-Phase Flows," *Int. J. Heat and Mass Trans.*, **42**, 3019 (1999).

Hibiki, T., and M. Ishii, "Interfacial Area Concentration in Steady Fully-Developed Bubbly Flow," *Int. J. Heat and Mass Trans.*, **44**, 3443 (2001).

Hills, J. H., "Radial Non-Uniformity of Velocity and Voidage in a Bubble Column," *Trans. Instn. Chem. Engrs.*, **52**, 1 (1974).

Hinze, J. O., *Turbulence*, McGraw-Hill, New York (1975).

Jacobsen, H. A., B. H. Sannaes, S. Grevskott, and H. F. Svendsen, "Modeling of Vertical Bubble Driven Flows," *Ind. Eng. Chem. Res.*, **36**, 4052 (1997).

Kocamustafaogullari, G., and M. Ishi, "Foundation of the Interfacial Area Transport Equation and its Closure Relations," *Int. J. Heat and Mass Transfer*, **38**, 481 (1995).

Krishna, R., M. I. Urseanu, J. M. van Baten, and L. Ellenberger, "Influence of Scale on the Hydrodynamics of Bubble Columns Operating in the Churn-Turbulent Regime: Experiments vs. Eulerian Simulations," *Chem. Eng. Sci.*, **54**, 4903 (1999).

Krishna, R., J. M. van Baten, and M. I. Urseanu, "Three Phase Eulerian Simulations of Bubble Column Reactors Operating in the Churn-Turbulent Regime: A Scale Up Strategy," *Chem. Eng. Sci.*, **55**, 3725 (2000).

Kuipers, J. A. M., and W. P. M. van Swaaij, "Computational Fluid Dynamics Applied to Chemical Reactor Engineering," *Adv. Chem. Eng.*, **24**, 227 (1998).

Lain, S., D. Bröder, and M. Sommerfeld, "Experimental and Numerical Studies of the Hydrodynamics in a Bubble Column," *Chem. Eng. Sci.*, **54**, 4913 (1999).

Lapin, A., and A. Lübbert, "Chaotic Flow in Bubble Column Reactors," *Chem. Eng. Sci.*, **50**, 2661 (1995).

Lapin, A., and A. Lübbert, "Fluid Dynamics in Bubble Column Bioreactors: Experiments and Numerical Simulation," *Biotechnol. and Bioeng.*, **52**, 248 (1996).

Lasheras, J. C., C. Martinez-Bazan, and J. L. Montanes, "On the Breakup of an Air Bubble Injected into a Fully Developed Turbulent Flow. Part 1. Breakup Frequency," *J. Fluid Mech.*, **401**, 157 (1999).

Lee, C. H., L. E. Erickson, and L. A. Glasgow, "Bubble Break-Up and Coalescence in Turbulent Gas-Liquid Dispersions," *Chem. Eng. Com.*, **59**, 65 (1987).

Levich, V. G., *Physicochemical Hydrodynamics*, Prentice-Hall, Englewood Cliffs, N. J. (1962).

Luo, H., and H. F. Svendsen, "Theoretical Model for Drop and Bubble Breakup in Turbulent Dispersions," *AIChE J.*, **42**, 1225 (1996).

Millies, M., and D. Mewes, "Liquid Circulation in Columns Due to Bubble Drift," *Chem. Eng. Technol.*, **15**, 258 (1992).

Millies, M., and D. Mewes, "Interfacial Area Density in Bubbly Flow," *Chem. Eng. Proc.*, **38**, 307 (1999).

Mudde, R. F., J. S. Groen, and H. E. A. Van Den Akker, "Liquid Velocity Field in a Bubble Column: LDA Experiments," *Chem. Eng. Sci.*, **52**, 4217 (1997).

Mudde, R. F., and O. Simonin, "Two- and Three-Dimensional Simulations of a Bubble Plume using a Two-Fluid Model," *Chem. Eng. Sci.*, **54**, 5061 (1999).

Pan, Y., M. P. Dudukovic, and M. Chang, "Dynamic Simulation of Bubbly Flow in Bubble Columns," *Chem. Eng. Sci.*, **54**, 2481 (1999).

Pan, Y., M. P. Dudukovic, and M. Chang, "Numerical Investigation of Gas-Driven Flow in 2D Bubble Columns," *AIChE J.*, **46**, 434 (2000).

Pfleger, D., S. Gomes, N. Gilbert, and H.-G. Wagner, "Hydrodynamic Simulations of Laboratory Scale Bubble Columns Fundamental Studies of the Eulerian-Eulerian Modelling Approach," *Chem. Eng. Sci.*, **54**, 5091 (1999).

Prince, M. J., and H. W. Blanch, "Bubble Coalescence and Break-up in Air-Sparged Bubble Columns," *AIChE J.*, **36**, 1485 (1990).

Ramkrishna, D., and A. W. Mahoney, "Population Balance Modelling. Promise for the Future," *Chem. Eng. Sci.*, **57**, 596 (2001).

Sato, Y., K. Sadatomi, and K. Sekoguchi, "Momentum and Heat Transfer in Two-Phase Bubbly Flow," *Int. J. Multiphase Flow*, **7**, 167 (1981).

Saynayal, J., S. Vasquez, S. Roy, and M. P. Dudukovic, "Numerical

Simulation of Gas-Liquid Dynamics in Cylindrical Bubble Column Reactors," *Chem. Eng. Sci.*, **54**, 5071 (1999).
Schrag, H. J., "Blasengröβen-Häufigkeitsverteilungen bei der Begasung von Gemischen organisch-chemischer Flüssigkeiten mit Stickstoff in Blasensäulen-Reaktoren," PhD Thesis, Universität Aachen, Germany (1976).
Sokolichin, A., G. Eigenberger, A. Lapin, and A. Lübbert, "Dynamic Numerical Simulation of Gas-Liquid Two-Phase Flows," *Chem. Eng. Sci.*, **52**, 661 (1997).
Sokolichin, A., and G. Eigenberger, "Applicability of the Standard k-ϵ Turbulence Model to the Dynamic Simulation of Bubble Columns. Part I: Detailed Numerical Simulations," *Chem. Eng. Sci.*, **54**, 2273 (1999).
Sokolichin, A., G. Eigenberger, O. Borchers, and C. Busch, "Applicability of the Standard k-ϵ Turbulence Model to the Dynamic Simulation of Bubble Columns. Part II: Comparison of Detailed Experiments and Flow Simulations," *Chem. Eng. Sci.*, **54**, 5927 (1999).
Thakre, S. S., and J. B. Joshi, "CFD Simulation of Bubble Column Reactors: Importance of Drag Force Formulation," *Chem. Eng. Sci.*, **54**, 5055 (1999).
Torvik, R., and H. F. Svendsen, "Modeling of Slurry Reactors, a Fundamental Approach," *Chem. Eng. Sci.*, **45**, 2325 (1990).
Valentas, K. J., and N. R. Amundson, "Breakage and Coalescence in Dispersed Phase Systems," *I&EC Fund.*, **5**, 533 (1966).
Walter, J. F., and H. W. Blanch, "Bubble Break-Up in Gas-Liquid Bioreactors: Break-Up in Turbulent Flows," *Chem. Eng. J.*, **32**, B7 (1986).
Webb, C., F. Que, and P. R. Senior, "Dynamic Simulation of Gas-Liquid Dispersion Behavior in a 2-D Bubble Column," *Chem. Eng. Sci.* **47**, 3305 (1992).
Wilkinson, P. M., "Physical Aspects and Scale-up of High Pressure Bubble Columns," PhD Thesis, University of Groningen, The Netherlands (1991).
Wilkinson, P. M., A. van Schayk, J. P. M. Spronken, and L. L. van Dierendonk, "The Influence of Gas Density and Liquid Properties on Bubble Breakup," *Chem. Eng. Sci.*, **48**, 1213 (1993).

Manuscript received May 17, 2001 and revision received Mar. 25, 2002.